2023 IEEE International Conference on Robotics and Automation (ICRA 2023)
May 29 - June 2, 2023. London, UK

Shape visual servoing of a tether cable from parabolic features

Lev Smolentsev[1], Alexandre Krupa[1], François Chaumette[1]

Abstract— **In this paper we propose a visual servoing approach that controls the deformation of a suspended tether cable subject to gravity from visual data provided by a RGB-D camera. The cable shape is modelled with a parabolic curve together with the orientation of the plane containing the tether. The visual features considered are the parabolic coefficients and the yaw angle of that plane. We derive the analytical expression of the interaction matrix that relates the variation of the visual features to the velocities of the cable extremities. Singularities are demonstrated to occur if and only if the cable is taut horizontally or vertically. An image processing algorithm is also developed to extract in real-time the current features fitting the parabola to the cable from the observed point cloud. Simulations and experimental results demonstrate the efficiency of our visual servoing approach to deform the tether cable toward a desired shape configuration.**

I. INTRODUCTION

The manipulation of Deformable Linear Objects (DLO) by a robotic manipulator is a challenging task due to the high number of DLO degrees of freedom (DOF) and the low number of robot DOF. Cable routing and cable inserting are common examples of DLO manipulation tasks in industry. Since these tasks are still mainly performed manually, their automation by robots has a great potential [8], [7], [6], [23]. In particular, two robot arms are used in [1] for manipulating a flexible beam in order to adapt its shape before an assembly operation. Accurately and automatically controlling the shape of a suspended cable can also be useful for Unmanned Aerial Vehicle (UAV) applications such as managing the shape of the power cable of tethered UAVs. For instance, [22] proposed a device composed of a winch mounted on the ground that is controlled to maintain the power cable in a slack configuration to avoid pulling the drone or touching the ground. [13] proposed an UAV controller that maintains the cable taut for canceling its oscillation and improving the flight stability. Another possible application is aerial transportation performed by a flying gripper made of two UAVs linked by a cable [5] or by cable-suspended parallel robots actuated by flying robots [4], [15]. Controlling the shape of power cables linking a chain of underwater robots was also considered in [11].

In the following, we present some works concerning the shape control of DLO using visual servoing. They are divided into two families: model-based and model-free approaches. In the model-free branch, the DLO is usually modeled as a set of points [1], [10], [19] or a contour [14] that can be represented by geometrical features. The common way to control the object deformation is by minimizing the error between the current measure of these features and their desired values corresponding to the targeted shape. In [1] the considered features are the 3D positions of markers attached on the DLO while in [10] a set of 3D equidistant points lying on a B-spline curve fitting the shape is considered. In [14] four different cases of features are studied: contour polynomial spline coefficients, Bezier and Nurbs splines control points, and Fourier coefficients. To relate the variation of these features to the velocities of the robot end-effector that interacts with the DLO, [1] propose to estimate an approximate shape Jacobian matrix during an offline identification procedure that consists in deforming the DLO by applying open-loop step motions on each robot DOF and measuring the induced displacements of the attached markers. The shape Jacobian matrix can also be estimated online from visual data by using a Kalman filter [14] or by minimizing a quadratic objective on a sliding time windows [10]. More recently, [16] proposed a control scheme relying on a shape Jacobian that is updated online from simulations based on a geometrical deformation model [17]. In another way, a neural network is trained in [19] during an offline procedure for predicting the shape Jacobian matrix from the position of the cable control points. All aforementioned works allow to control the shape of the DLO without knowledge of its mechanical properties. However, the limitations of these approaches are the inability to determine possible singular configurations of the system that may cause instabilities in the control and the potential convergence of the system to local minima if the goal configuration is too far away. Moreover, the approaches that require an online estimation of the shape Jacobian are sensitive to measurement noise.

In the model-based branch of methods, a way to control the shape of a soft body consists in using a mechanical model that predicts its behavior. However, depending of its complexity, it may be difficult to run this model in real-time. The authors of [9] consider control points velocities as features and use a Finite Element Model that formulates locally the static equilibrium equations for these points to avoid real-time model simulations. In some cases the control input can be derived directly from model equations as it is done in [5] and [11] with a catenary/chain curve.

In this work, we focus on the robotic manipulation of a suspended tether cable that is subject to gravity in order to control its shape. In that case, the cable can be slack or

This work carried out in the MAMBO project has received a French government support granted to the Labex CominLabs excellence laboratory and managed by the National Research Agency in the "Investing for the Future" program under reference ANR-10-LABX-07-01

Experiments presented in this paper were carried out thanks to a platform of the Robotex 2.0 French research infrastructure

[1]L. Smolentsev, A. Krupa, and F. Chaumette are with Inria, Univ Rennes, CNRS, IRISA, Campus de Beaulieu, 35042 Rennes, France Firstname.Name@inria.fr

taut and we propose to generalize this possible set of configurations in a single and simple geometrical model: a 2^{nd} order polynomial curve, that is, a parabola. We show through simulations and experimental results that such approximation is sufficient. The proposed shape control approach only uses the length of the cable as *a priori* knowledge and the visual information provided by a RGB-D camera observing the cable. Moreover, it is capable of operating with slack and taut configurations and does not need to observe the cable extremities. In particular, the chain model considered in [11] and in [5] does not allow to consider any taut configurations due to a singularity of the corresponding shape Jacobian, while our parabola model is not singular in this configuration apart when the cable is taut horizontally or vertically. An analytic expression of the shape Jacobian is derived for this model, thus avoiding the limitations of the model-free methods mentioned earlier. Another advantage of our solution is that it does not consider any mechanical model of the DLO and thus does not need any knowledge about its material mechanical properties. In contrast, our method relies only on an approximate geometrical model that is extracted and tracked from RGB-D data.

The paper is organized as follows: Section II presents the selected model of the tether cable and the visual features proposed for controlling its shape. The related Shape Jacobian matrix is analytically derived, from which a complete singularity analysis is performed and a classical visual servoing controller is presented. Section III describes the image processing developed to track in real-time the cable shape from the successive 3D point clouds provided by a RGB-D camera. Section IV presents simulation and experimental results of the proposed visual servoing approach. Finally, Section V summarizes the results of our work.

II. Polynomial Visual Servoing

A. Tether Modelling

We begin by defining Cartesian frames and 3D points necessary to model the tether shape. Coordinate frames are shown on Fig. 1. Note that both the tether frame $\mathcal{F}_t$ and the world frame $\mathcal{F}_w$ are defined so that their z axis is in the opposite direction of the gravity. Points p_m and p_f represent tether attachment points and p_m is selected as the origin of $\mathcal{F}_t$. To be as general as possible, we consider in this section that both the 3D positions of p_m and p_f can be controlled.

Since the system has 3 degrees of freedom (that are the 3 components of the relative translation between p_m and p_f), 3 independent parameters are sufficient to control it. Let us note that a trivial solution would be to select as visual features the relative position between p_m and p_f. However, these two points may not be visible. That is why the method we propose does not necessitate to measure their 3D coordinates. As already said, we use a parabola to model the shape of the cable. Its equation in the plane (x_t, z_t) to which it belongs is given by $z = ax^2 + bx$. We thus use as first two visual features the parameters a and b that characterize the shape of this parabola. Finally and similarly to [11], we use as third and last feature the yaw angle of the vertical plane containing the cable, *i.e.*, the angle α between x_t and x_w (note that $\sin\alpha$ was used in [11], which induces a singularity when $\alpha = \pm\pi/2$).

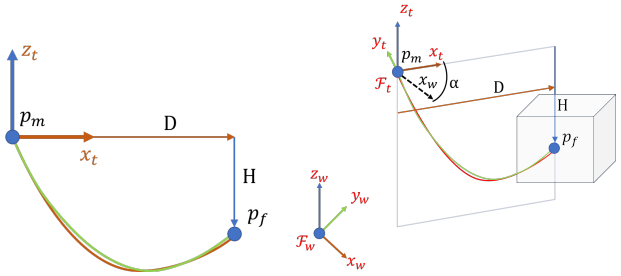

(a) Side view (b) Isometric view

Fig. 1: Tether (green curve) and its parabola model (red curve): $D > 0$, $H < 0$ in this configuration.

In frame $\mathcal{F}_t$ the coordinates $\mathbf{p}_m$ and $\mathbf{p}_f$ are respectively given by $(0,0,0)$ and $(D,0,H)$ and any point belonging to the parabola that represents the tether has as coordinates:

$$ {}^t\mathbf{p} = \begin{pmatrix} {}^t x \\ 0 \\ a\ {}^t x^2 + b\ {}^t x \end{pmatrix} \tag{1} $$

where $H = aD^2 + bD$. Since $\mathcal{F}_t$ and $\mathcal{F}_w$ have been defined with parallel $\mathbf{z}$ axis, their relative pose is given by the homogeneous transformation matrix (c stands for cos, s for sin):

$$ {}^w\mathbf{H}_t = \begin{bmatrix} c\alpha & -s\alpha & 0 & {}^w p_{m_x} \\ s\alpha & c\alpha & 0 & {}^w p_{m_y} \\ 0 & 0 & 1 & {}^w p_{m_z} \\ 0 & 0 & 0 & 1 \end{bmatrix} \tag{2} $$

This allows expressing any tether point in $\mathcal{F}_w$ by:

$$ {}^w\mathbf{p} = {}^w\mathbf{p}_m + \begin{pmatrix} {}^t x\ c\alpha \\ {}^t x\ s\alpha \\ a\ {}^t x^2 + b\ {}^t x \end{pmatrix} \tag{3} $$

In particular, the coordinates of point p_f in $\mathcal{F}_w$ is given by:

$$ {}^w\mathbf{p}_f = {}^w\mathbf{p}_m + \begin{pmatrix} D\ c\alpha \\ D\ s\alpha \\ aD^2 + bD \end{pmatrix} \tag{4} $$

B. Interaction matrix

As already said, the set $\mathbf{s}$ of visual features we consider is:

$$ \mathbf{s} = \begin{pmatrix} a \\ b \\ \alpha \end{pmatrix} \tag{5} $$

We are now interested in determining the time variation of $\mathbf{s}$ in function of the time variation of ${}^w\mathbf{p}_m$ and ${}^w\mathbf{p}_f$ in $\mathcal{F}_w$ for obtaining the analytical form of the interaction matrix of $\mathbf{s}$. By differentiating (4) we obtain:

$$ {}^w\dot{\mathbf{p}}_f = {}^w\dot{\mathbf{p}}_m + \begin{pmatrix} \dot{D}c\alpha - s\alpha D\dot{\alpha} \\ \dot{D}s\alpha + c\alpha D\dot{\alpha} \\ (2aD + b)\dot{D} + D^2\dot{a} + D\dot{b} \end{pmatrix} \tag{6} $$

This equation can be rewritten as:

$$ {}^w\dot{\mathbf{p}}_f - {}^w\dot{\mathbf{p}}_m = \begin{bmatrix} 0 & 0 & c\alpha & -Ds\alpha \\ 0 & 0 & s\alpha & Dc\alpha \\ D^2 & D & 2aD+b & 0 \end{bmatrix} \begin{pmatrix} \dot{a} \\ \dot{b} \\ \dot{D} \\ \dot{\alpha} \end{pmatrix} \quad (7) $$

As D depends on a and b, it is necessary to eliminate $\dot{D}$ from (7) to get a one-to-one relation between $\dot{\mathbf{s}}$ and ${}^w\dot{\mathbf{p}}_f - {}^w\dot{\mathbf{p}}_m$. In frame $\mathcal{F}_t$, D is related to a, b and the tether length L by the following equation:

$$ L = \int_0^D \sqrt{1+(2ax+b)^2}dx \quad (8) $$

To solve this integral analytically, we choose $t = 2ax + b$, from which we deduce $dt = 2adx$ and we obtain:

$$ L = \frac{1}{2a}\int_{t_1}^{t_2} \sqrt{1+t^2}dt \quad (9) $$

where $t_1 = b$ and $t_2 = 2aD + b$. Notice that this equation is not valid when $a = 0$ (that is, when the parabola degenerates to a straight line, in which case the tether is taut) for which:

$$ L = D\sqrt{1+b^2} = \sqrt{D^2+H^2} \quad (10) $$

Since it is well known that:

$$ \int \sqrt{1+t^2}dt = \frac{1}{2}t\sqrt{1+t^2} + \frac{1}{2}\ln\left|t+\sqrt{1+t^2}\right| \quad (11) $$

and

$$ \ln\left|t+\sqrt{1+t^2}\right| = \operatorname{arcsinh} t, t \in \mathbb{R} \quad (12) $$

we finally obtain the expression of the tether length:

$$ \begin{aligned} L &= f(D,a,b) \\ &= \Big(t_2\sqrt{1+t_2^2} - b\sqrt{1+b^2} \\ &+ \operatorname{arcsinh} t_2 - \operatorname{arcsinh} b\Big)/(4a) \end{aligned} \quad (13) $$

Since $\dot{L} = 0$, by differentiating (13) we get:

$$ \frac{\partial f}{\partial D}\dot{D} = -\frac{\partial f}{\partial a}\dot{a} - \frac{\partial f}{\partial b}\dot{b} \quad (14) $$

from which we obtain:

$$ \dot{D} = k_1\dot{a} + k_2\dot{b} \quad (15) $$

where

$$ k_1 = 4(L - D\sqrt{1+t_2^2})/k \quad (16) $$

$$ k_2 = 2(\sqrt{1+b^2} - \sqrt{1+t_2^2})/k \quad (17) $$

with

$$ k = 4a\sqrt{1+t_2^2} \quad (18) $$

We can note that $k = 0$ when $a = 0$ (*i.e.,* the tether is taut). Fortunately, after applying a first order Taylor expansion to the term $f(a) = \sqrt{1+t_2^2} = \sqrt{1+(2Da+b)^2}$, we obtain

$$ \lim_{a\to 0} k_1 = \frac{-2D^2b}{1+b^2} \quad (19) $$

$$ \lim_{a\to 0} k_2 = \frac{-Db}{1+b^2} \quad (20) $$

It is thus always possible to compute the terms k_1 and k_2 whatever the tether configuration. Then by injecting (15) into (7) we obtain the following relation:

$$ {}^w\dot{\mathbf{p}}_f - {}^w\dot{\mathbf{p}}_m = \mathbf{M}\dot{\mathbf{s}} \quad (21) $$

with

$$ \mathbf{M} = \begin{bmatrix} k_1c\alpha & k_2c\alpha & -Ds\alpha \\ k_1s\alpha & k_2s\alpha & Dc\alpha \\ n_1 & n_2 & 0 \end{bmatrix} \quad (22) $$

where $n_1 = D^2 + t_2k_1$ and $n_2 = D + t_2k_2$. The inverse of $\mathbf{M}$ can be analytically calculated and is given by:

$$ \mathbf{M}^{-1} = \frac{1}{Dq}\begin{bmatrix} -n_2c\alpha & -n_2s\alpha & k_2 \\ n_1c\alpha & n_1s\alpha & -k_1 \\ -qs\alpha & qc\alpha & 0 \end{bmatrix} \quad (23) $$

with $q = Dk_2 - k_1$.
From (21), we finally obtain the relation:

$$ \dot{\mathbf{s}} = \mathbf{M}^{-1}({}^w\dot{\mathbf{p}}_f - {}^w\dot{\mathbf{p}}_m) = \mathbf{L_s}\mathbf{v} \quad (24) $$

where $\mathbf{L_s} = \begin{bmatrix} -\mathbf{M}^{-1} & \mathbf{M}^{-1} \end{bmatrix}$ is the 3×6 shape interaction matrix that relates the variation of the visual features $\mathbf{s}$ to the translational velocity of p_m and p_f expressed in $\mathcal{F}_w$: $\mathbf{v} = (\mathbf{v}_m, \mathbf{v}_f) = ({}^w\dot{\mathbf{p}}_m, {}^w\dot{\mathbf{p}}_f)$

C. Control law

From the modelling presented in the previous section, we can immediately use the classical control law:

$$ \mathbf{v} = -\lambda\mathbf{L}_\mathbf{s}^+(\mathbf{s} - \mathbf{s}^*) \quad (25) $$

for ensuring an exponential decrease of the visual feature error $\mathbf{e} = \mathbf{s} - \mathbf{s}^*$ toward zero [2]. Here $\mathbf{s}^*$ denotes the desired value of the visual features, $\lambda(> 0)$ is the control gain, and $\mathbf{L}_\mathbf{s}^+$ is the Moore-Penrose pseudoinverse of $\mathbf{L_s}$. In case point p_f is static (which is the case considered for our real experiments), the controller reduces to:

$$ \mathbf{v}_m = \lambda\mathbf{M}(\mathbf{s} - \mathbf{s}^*) \quad (26) $$

Note that apart the singular configurations exhibited in Section II-D, $\mathbf{M}$ is always of full rank 3, which ensures that the system is globally asymptotically stable in case $\mathbf{M}$ is correctly evaluated in (25) [2].

As can be seen from (22), matrix $\mathbf{M}$ depends on the visual features a, b, α that are measured at each iteration of the control scheme, the tether length L that is constant and supposed to be known, and D that is varying. We thus need to estimate D. There are two ways for that: the first would be to track the attachment points p_f and p_m and measure their 3D position. As already said, this would not be convenient because the camera would need to have both points in its field of view, which would reduce the range of possible applications. The second method relies on estimating D from (13). Since there is unfortunately no explicit form for the solution of this equation, we propose to numerically search for a zero of (13):

$$ D = \underset{D\in\mathbb{R}}{\operatorname{argmin}}\left(f(D,a,b) - L\right) \quad (27) $$

by determining D with a Newton method using the derivatives of the objective function (27). In practice, only a couple of iterations are needed to estimate the new value of D at each iteration of the control loop by using its previous value as initial guess. We used $D = L/2$ for the very first image.

D. Study of the singularities of $\mathbf{L_s}$

In the following, we present a study on the possible singularities that the interaction matrix $\mathbf{L_s}$ may encounter. The determinant of $\mathbf{M}$ is given by:

$$\det \mathbf{M} = D^2 q = D^2(Dk_2 - k_1) \tag{28}$$

$\mathbf{M}$ and thus $\mathbf{L_s}$ are singular when D is null, meaning that points p_f and p_m coincide or lay on the same vertical. This is logical since the angle α is no more defined in that degenerate case. Another singularity is reached for the condition $Dk_2 - k_1 = 0$. By using (16) and (17) this condition can be rewritten as:

$$D(\sqrt{1+\tan^2\alpha_f} + \sqrt{1+\tan^2\alpha_m}) = 2L \tag{29}$$

with $\tan\alpha_f = t_2 = 2Da + b$ and $\tan\alpha_m = b$, where α_f and α_m are respectively the angles of the tangent of the parabola at point p_m and p_f (see Fig. 2).

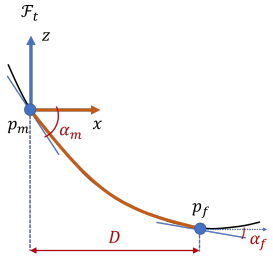

Fig. 2: Tangent of the parabola at points p_m and p_f.

Since $1 + \tan^2\alpha = \frac{1}{\cos^2\alpha}$, (29) is equivalent to

$$\frac{D}{|\cos\alpha_f|} + \frac{D}{|\cos\alpha_m|} = 2L \tag{30}$$

Then, by combining (30) and (13), and using $\tan\alpha_f - \tan\alpha_m = 2Da$, we obtain:

$$\frac{\tan\alpha_f}{|\cos\alpha_m|} - \frac{\tan\alpha_m}{|\cos\alpha_f|} = \operatorname{arcsinh}\left(\frac{\tan\alpha_f}{|\cos\alpha_m|} - \frac{\tan\alpha_m}{|\cos\alpha_f|}\right) \tag{31}$$

The singularity condition is given by the solution of (31), which exists in $\mathbb{R}$ if and only if

$$\frac{\tan\alpha_f}{|\cos\alpha_m|} = \frac{\tan\alpha_m}{|\cos\alpha_f|} \tag{32}$$

Thus, the singularity occurs when $\alpha_m = \alpha_f$, meaning that the tether is taut. However, when the tether is taut, we directly obtain from (19) and (20) $q = Dk_2 - k_1 = D^2 b/(1+b^2)$. Apart from the previous exhibited configuration $D = 0$, this term vanishes only when $b = 0$, that is, when the tether is taut horizontally.

This analysis demonstrates two singular configurations only: when p_f and p_m coincide, and when the parabola degenerates into a vertical or horizontal straight line. The former configuration corresponds to a pure degenerate case that cannot occur in practice. The latter can be avoided by never specifying such a desired configuration.

III. Features extraction

In practice, the tether shape is estimated from RGB-D data. In particular, its RGB image together with the depth are used to fit a parabola into the observed point cloud of the tether. The image processing pipeline consists in first applying an HSV threshold on the RGB image to segment the cable in the image from its color (yellow in our case). A thinning algorithm [21] is then applied for determining the middle line of the cable in the image. The 3D coordinates of the N points belonging to this middle line are first expressed in the camera frame $\mathcal{F}_c$ thanks to the depth data (see Fig. 3) and then in the world frame $\mathcal{F}_w$ thanks to the knowledge of the transformation matrix ${}^w\mathbf{H}_c$ (determined offline using a classical hand-eye calibration technique [18]). Using these 3D points ${}^w\mathbf{p}_1 \dots {}^w\mathbf{p}_N$, the parameters ${}^w\mathbf{n}$ and ${}^w d$ of the cable plane equation ${}^w\mathbf{n}^T\,{}^w\mathbf{p} + {}^w d = 0$ in $\mathcal{F}_w$ are estimated by using a robust least square method [3] for eliminating potential outliers due to depth measurement errors. Notice that we impose the z-component of the normal ${}^w\mathbf{n}$ to ${}^w n_z = 0$ during the estimation process since the plane is always vertical in $\mathcal{F}_w$ due to the gravity. The angle α is then directly given by:

$$\alpha = \arctan(-{}^w n_x / {}^w n_y) \tag{33}$$

Afterwards, we use the cable plane equation expressed in the camera frame $\mathcal{F}_c$: ${}^c\mathbf{n}^T{}^c\mathbf{p} + {}^c d = 0$ to reconstruct the 3D coordinates ${}^c\mathbf{p}_i$ of each point belonging to the middle line of the cable from its observed image coordinates $\mathbf{p}_{im} = (\tilde{x}_i, \tilde{y}_i, 1)$. Indeed, we have:

$${}^c\mathbf{p}_i = (\tilde{x}_i z_i, \tilde{y}_i z_i, z_i) \tag{34}$$

with

$$z_i = -\frac{{}^c d}{{}^c\mathbf{n}^T \mathbf{p}_{im}} \tag{35}$$

This process allows considering a new set of N 3D points that are less tainted by the sensor depth measurement noise. Note that ${}^c\mathbf{n}^T\mathbf{p}_{im} = 0$ in (35) if and only if the cable plane is orthogonal to the image plane, which is a degenerate case we do not consider. Finally, the parabolic features a and b are estimated using a classical least squares method from this set of N points expressed in $\mathcal{F}_t$. For doing that, the points are expressed in $\mathcal{F}_t$ using the transformation ${}^t\mathbf{H}_c = {}^t\mathbf{H}_w\,{}^w\mathbf{H}_c$ where ${}^t\mathbf{H}_w$ is the inverse of the homogeneous transformation (2) that is computed using the estimated α and the 3D position of p_m in $\mathcal{F}_w$ provided by the robot odometry. Furthermore, a and b are given by solving $a\,{}^t x_i^2 + b\,{}^t x_i = {}^t z_i, i = 1, \dots, N$ whose solution is given by:

$$\begin{bmatrix} a \\ b \end{bmatrix} = \begin{bmatrix} {}^t x_1^2 & {}^t x_1 \\ \dots & \dots \\ {}^t x_N^2 & {}^t x_N \end{bmatrix}^+ \begin{bmatrix} {}^t z_1 \\ \dots \\ {}^t z_N \end{bmatrix} \tag{36}$$

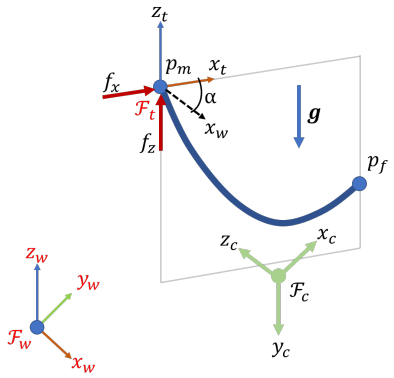

Fig. 3: The tether cable setup used for the simulations and the experiments. The external forces used in the simulation are depicted in red.

Note that at least two points are necessary to obtain a and b, but the more the better.

IV. Results

In a first part, we test our control approach in a simulation framework by using a continuous mechanical model of the tether cable to simulate its deformation. The accompanying video shows simulations where the position of the two cable extremities are controlled. In a second part, we present experimental results obtained for the real system and show that our method is robust to the approximation of the tether by a parabolic curve. Note that there is no difference between eye-in-hand and eye-to-hand setups in our case since the pose of the camera frame $\mathcal{F}_c$ with respect to the world frame $\mathcal{F}_w$ is constant and known from hand-eye calibration for the eye-to-hand setup while this now varying pose is obtained from hand-eye calibration and robot odometry for the eye-in-hand setup.

A. Simulation framework

A simulation framework has been implemented for validating the control approach developed in Section II. The overall pipeline of the simulation is presented by Algorithm 1 where dk is the simulation time step. For simulating a realistic cable deformation, the shape of the tether is expressed following the extensible catenary model presented in [20]. For using this model, we set arbitrary values for the Young's modulus E, the tether cross-section A and the tether mass per unit length ρ. These parameters correspond to the mechanical parameters of the cable that are required for the physics-based model [20]. From the known position of the two tether extremities, the corresponding external force $\mathbf{f}$ with components $(f_x, 0, f_z)$ in $\mathcal{F}_t$ to be applied to the extremity point p_m is first estimated (see Fig. 3). Then, the solution at static equilibrium of the forces applied to the tether, that is, the external force $\mathbf{f}$ and the gravity $\mathbf{g}$, allows determining the shape of the cable, from which a Point Cloud (PC) is generated. The coefficients (a, b) of the parabola are then determined using the least squares method described in Section III and a next iteration of the control loop can be

while $||\mathbf{e}_k|| > \epsilon$ **do**
- $\mathbf{e}_k = \mathbf{s}_k - \mathbf{s}^*$
- compute D from (27)
- compute $\mathbf{M}(\mathbf{s}_k, D, L)$ from (22)
- $\mathbf{v}_m = \lambda \mathbf{M} \mathbf{e}_k$
- ${}^w\mathbf{p}_{m(k+dk)} = {}^w\mathbf{p}_{m(k)} + \mathbf{v}_m dk$
- compute α from ${}^w\mathbf{p}_{m(k+dk)}$ and ${}^w\mathbf{p}_f$
- compute ${}^w\mathbf{H}_t$ from (2)
- $\mathbf{f}$ = simulator.estimateF(${}^t\mathbf{p}_m, {}^t\mathbf{p}_f, E, A, \rho$)
- cable PC = simulator.sampleCatenary($\mathbf{f}, E, A, \rho$)
- compute a, b from cable PC
- $\mathbf{s}_k = (a, b, \alpha)$

end

Algorithm 1: Simulation of the proposed visual servoing

achieved. We use ViSP [12] for the implementation of the overall simulation.

The results of two shape servoing tasks are illustrated on Fig. 4. The first one is such that $\mathbf{s}^* = [0, -0.7, 0]$, which means we want to reach a taut configuration, while the second one is such that $\mathbf{s}^* = [3.6, -1, -30^o]$, which corresponds to a general configuration. In both cases, the initial configuration of the tether is set to $\mathbf{s}_0 = [1.2, -1.4, 75°]$. We can see the perfect exponential decrease of the error on Fig. 4c and 4d. The three translational velocities of p_m depicted on Fig. 4e and 4f also show a nice behavior without any instabilities when the tether becomes taut. These simulation results demonstrate that our control solution based on an approximation of the tether shape with a parabola can accurately perform the task, whatever the desired configuration of the cable.

B. Experimental validation

The experimental setup is composed by an Omron© 6 DOF articulated robot Viper650 (see Fig. 5a). The left extremity of a 86 centimeters length cable is attached to the robot end-effector and the right one is fixed to a tripod. A remote Intel© D435 RGB-D with a resolution of 1280x720 pixels for both data streams is mounted on a second fixed tripod and observes the scene.

To validate our method two different tasks were tested: the first is to stretch the tether by setting $\mathbf{s}^* = [0, -0.4, -30°]$ and the second is to move it back to a slack configuration with $\mathbf{s}^* = [1.5, -1.4, -15°]$. The initial state is such that $\mathbf{s}_0 = [1, -1.1, -17°]$. The robot control sampling frequency is set to the camera frame rate (30 Hz) and the control gain to $\lambda = 0.5$. Typical RGB and depth images acquired by the camera are presented in Fig. 5. The temporal evolution of the features error together with the control velocity applied on point p_m are shown on Fig. 6 (see also the accompanying video). One can see in Fig. 6a and 6b the exponential decoupled decrease of the features error to zero, which demonstrates the efficiency of the proposed approach. We can note on Fig. 6c and 6d that the noise on the estimated value of α, which is due to the low accuracy of the depth measurements, induces some noise on the v_x

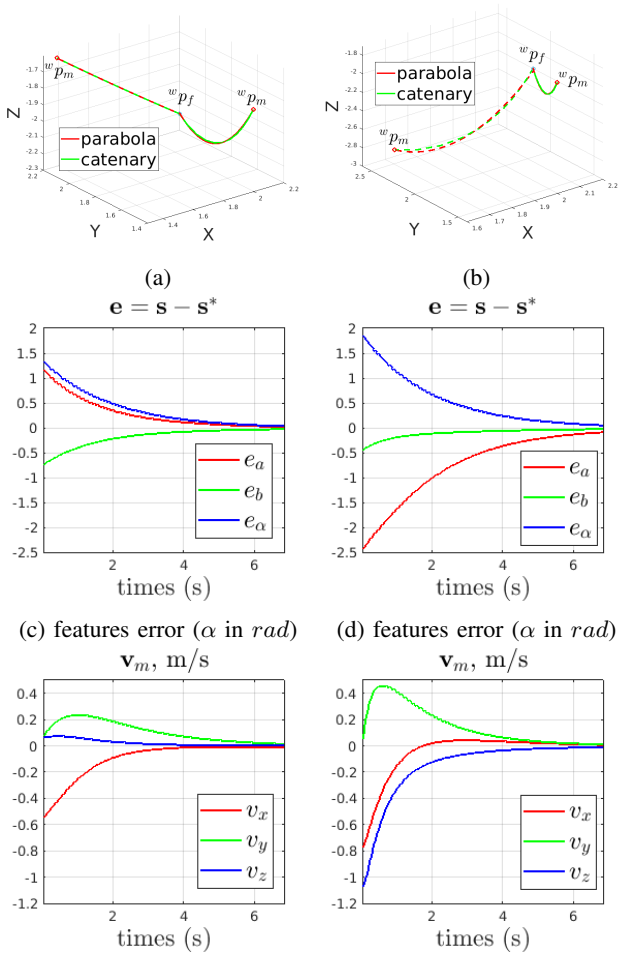

Fig. 4: Simulation results. Cable configuration at the beginning and at the end for the first task (a) and for the second task (b) (parabola depicted in red and catenary in green). Evolution of the visual features error (c),(d) and velocity applied to point $\mathbf{p}_m$ (e),(f) during the first and the second tasks respectively.

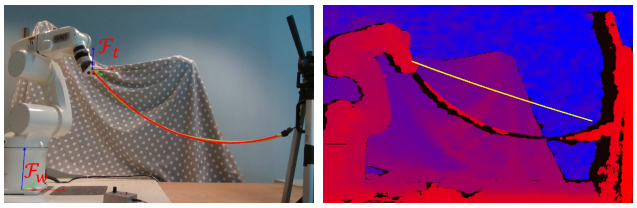

Fig. 5: (a) RGB image of the experiment during the first task. The fitted parabola, $\mathcal{F}_w$ and $\mathcal{F}_t$ frames are depicted in red. (b) Depth image with the first task target shape overlaid in yellow.

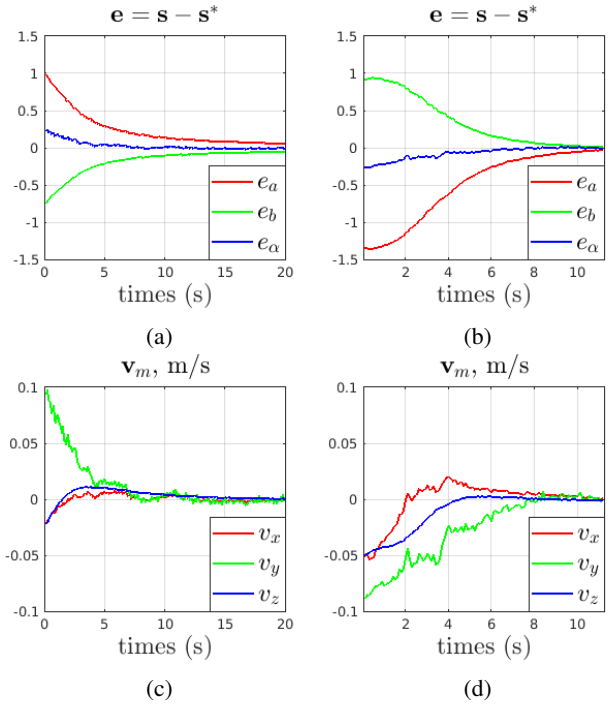

Fig. 6: Evolution of the visual features error during Task 1 (a) and Task 2 (b). Applied control velocity $\mathbf{v}_m$ during Task 1 (c) and Task 2 (d). For features units refer to Fig. 4c.

and v_y components of the end-effector velocity, but without destabilizing the system. These results show that even if our approach is based on a coarse modelling of the tether cable by a parabolic curve, it can efficiently perform the shaping task thanks to the robustness of the shape servoing closed-loop control scheme.

V. Conclusion

In this paper, we addressed the automatic manipulation of a suspended tether cable. We proposed three visual features from a simple parabolic geometric model to control the translational velocities of its extremities. The analytical form of the related interaction matrix has been determined, allowing to demonstrate the absence of singularities apart when the tether is taut vertically or horizontally. Simulations together with real world tests have shown the efficiency of our method that does not require any knowledge of material mechanical properties. In comparison to model-free methods, the proposed approach has the advantage to provide a complete study of potential singular configurations and it gets rid of an online estimation of the shape Jacobian. Moreover it does not require any path planning for local minima avoidance and allows to bring the cable to taut configurations, which was not possible before.

In future work, we plan to extend this approach for controlling two quadrotors holding together a tether cable with the objective to grasp and manipulate objects for transport applications.

VI. Acknowledgements

The authors would like to thank Sébastien Briot who suggested to use the catenary model for simulations, as well as Isabelle Fantoni for useful discussions.

REFERENCES

[1] S. Caro, C. Chevallereau, and A. Remus. Manipulating deformable objects with a dual-arm robot. In *2nd Int. Conf. on Robotics, Computer Vision and Intelligent Systems (ROBOVIS)*, pages 48–56, 2021.

[2] F. Chaumette, S. Hutchinson, and P. Corke. Visual servoing. In O. Khatib B. Siciliano, editor, *Handbook of Robotics, 2nd edition*, pages 841–866. Springer, 2016.

[3] A. Comport, E. Marchand, and F. Chaumette. Robust model-based tracking for robot vision. In *IEEE/RSJ Int. Conf. on Intelligent Robots and Systems (IROS)*, pages 692–697, 2004.

[4] J. B. Czapalay Erskine, A. Chriette, and S. Caro. Wrench capability analysis of aerial cable towed systems. In *ASME Int. Design Engineering Technical Conf. & Computers and Information in Engineering Conf. (IDETC/CIE)*, 2018.

[5] D. S. D'Antonio, G. A. Cardona, and D. Saldana. The catenary robot: Design and control of a cable propelled by two quadrotors. *IEEE Robotics and Automation Letters*, 6(2):3857–3863, April 2021.

[6] P. M. Fresnillo, S. Vasudevan, and W. M. Mohammed. An approach for the bimanual manipulation of a deformable linear object using a dual-arm industrial robot: cable routing use case. In *IEEE 5th Int. Conf. on Industrial Cyber-Physical Systems (ICPS)*, 2022.

[7] K. Galassi and G. Palli. Robotic wires manipulation for switchgear cabling and wiring harness manufacturing. In *IEEE 4th Int. Conf. on Industrial Cyber-Physical Systems (ICPS)*, pages 531–536, 2021.

[8] S. Jin, W. Lian, Ch. Wang, M. Tomizuka, and S. Schaal. Robotic cable routing with spatial representation. *IEEE Robotics and Automation Letters*, 7(2):5687–5694, April 2022.

[9] A. Koessler, N. Roca Filella, B.C. Bouzgarrou, L. Lequièvre, and J.-A. Corrales Ramon. An efficient approach to closed-loop shape control of deformable objects using finite element models. In *IEEE Int. Conf. on Robotics and Automation (ICRA)*, pages 1637–1643, 2021.

[10] R. Lagneau, A. Krupa, and M. Marchal. Automatic shape control of deformable wires based on model-free visual servoing. *IEEE Robotics and Automation Letters*, 5(4):5252–5259, October 2020.

[11] M. Laranjeira, C. Dune, and V. Hugel. Catenary-based visual servoing for tether shape control between underwater vehicles. *Ocean Engineering*, 200, 2020.

[12] E. Marchand, F. Spindler, and F. Chaumette. Visp for visual servoing: a generic software platform with a wide class of robot control skills. *IEEE Robotics and Automation Magazine*, 12(4):40–52, December 2005.

[13] M. M. Micotra, R. Naldi, and E. Garone. Taut cable control of a tethered uav. In *19th World Congress The Int. Federation of Automatic Control*, volume 47, pages 3190–3195, 2014.

[14] J. Qi, W. Ma, and D. Navarro-Alarcon. Adaptive shape servoing of elastic rods using parameterized regression features and auto-tuning motion controls. In *IEEE/RSJ Int. Conf. on Intelligent Robots and Systems (IROS)*, pages 353–354, 2020.

[15] D. Sanalitro, M. Tognon, A.E. Jimenez Cano, J. Cortés, and A. Franchi. Indirect force control of a cable-suspended aerial multi-robot manipulator. *IEEE Robotics and Automation Letters*, 7(3):6726–6733, July 2022.

[16] M. Shetab-Bushehri, M. Aranda, Y Mezouar, and E Özgür. As-rigid-as-possible shape servoing. *IEEE Robotics and Automation Letters*, 7(2):3898–3905, April 2022.

[17] O. Sorkine and M. Alexa. As-Rigid-As-Possible Surface Modeling. In *Eurographics Symp. on Geometry Processing*, pages 109–116, 2007.

[18] R. Tsai. A versatile camera calibration technique for high-accuracy 3d machine vision metrology using off-the-shelf tv cameras and lenses. *IEEE Journal on Robotics and Automation*, 3(4):323–344, August 1987.

[19] M. Yu, H. Zhong, and X. Li. Shape control of deformable linear objects with offline and online learning of local linear deformation models. In *IEEE Int. Conf. on Robotics and Automation (ICRA)*, pages 1337–1343, 2022.

[20] H. Yuan, E. Courteille, and D. Deblaise. Static and dynamic stiffness analyses of cable-driven parallel robots with non-negligible cable mass and elasticity. *Mechanism and Machine Theory*, 85:64–81, 2015.

[21] T. Y. Zhang and C. Y. Suen. A fast parallel algorithm for thinning digital patterns. *Communications of the ACM*, 27(3):236–239, 1984.

[22] L. Zikou, C. Papachristos, and A. Tzes. The power-over-tether system for powering small uavs: Tethering-line tension control synthesis. In *23rd Mediterranean Conf. on Control and Automation (MED)*, pages 681–687, 2015.

[23] M. Zürn, M. Wnuk, A. Lechler, and A. Verl. Software architecture for deformable linear object manipulation: A shape manipulation case study. In *IEEE/ACM 4th Int. Workshop on Robotics Software Engineering (RoSE)*, pages 9–16, 2022.